

Characterising the Internal Wave Dynamics of Barkley Canyon (Rough)

Kurtis Anstey

V00939802

Department of Physics and Astronomy

University of Victoria

May 19, 2021

Dr. Jody Klymak (University of Victoria)

Dr. Steven Mihal (Ocean Networks Canada)

Dr. Richard Thomson (Institute of Ocean Sciences)

Table of Contents

List of Figures	3
1 Abstract	4
2 Introduction	5
3 Theory	8
4 Data	10
5 Methods	13
5.1 Velocities	13
5.2 Power spectral density	13
5.3 Rotary spectra	16
5.4 Spectrograms	17
5.5 Depth-band integrated power	18
5.6 Critical slope analysis	19
6 Results	20
6.1 Seasonality	20
6.2 Slope effects	21
6.3 Canyon effects	26
6.4 Continuum analysis	26
7 Discussion	26
8 Conclusions	26
9 References	27

List of Figures

1	Internal wave processes	6
2	Internal waves and topography	7
3	Radiating internal waves in a lab	9
4	Bathymetry of Barkley Canyon	11
5	Site topography	12
6	Velocities - 2013	14
7	Power spectra - 2013	15
8	Rotary spectra - 2013	16
9	Spectrograms (PSD) - 2013	17
10	Spectrograms (rotary) - 2013	18
11	Averaged stratification and WKB-stretch scaling	20
12	Depth-band PSD - Upper Slope - 2013	22
13	Depth-band rotary spectra - Upper Slope - 2013	24

1 Abstract

This research characterises the internal wave field at Barkley Canyon, to provide information regarding regional mixing processes and what drives them. We make use of four overlapping years of ADCP time-series data, at both slope and canyon sites, to build on a body of research regarding interactions of internal waves with irregular topography, and associated processes, in the Vancouver Island Continental Shelf (VICS) region. This research is important for understanding transport of nutrients, heat, O_2 , and CO_2 , which affect climate drivers like the overturning circulation, as well as biological productivity. Key findings indicate that individual frequency constituents and bands experience unique seasonality, near-slope intensification, and canyon effects. Additionally, a topographically influenced internal wave continuum state, as compared to canonical GM79 theory, could further influence slope and canyon mixing contributions.

2 Introduction

Internal waves are slow-moving, low-frequency, underwater gravity waves that exist due to density gradients in the ocean interior (Garrett & Munk, 1979). They can have wavelengths up to kilometres long, and oscillate in a range between the Coriolis (inertial, f) and Brunt–Väisälä (buoyancy, N) frequencies (Garrett & Munk, 1979). They are caused by wind, or tides and currents moving over irregular seafloor topography, generating waves that travel through the stratified ocean (Hendershott & Garrett, 2018). These waves propagate through the depths, where incident topography can cause them to scatter, reflect, or break (Martini et al., 2013).

As the wind and tides are ever-present drivers of ocean processes, internal waves are common features. As early as the mid-19th century, scientists such as Stokes and Rayleigh were discussing fluid density and stratification, essential for internal wave propagation (Garrett & Munk, 1979). Internal waves were reported as consistent noise in early 20th-century hydrocast readings, and Ekman made note of them in his seminal theories on fluid mechanics (Garrett & Munk, 1979). Later, Garrett and Munk (1979) developed the canonical Garrett-Munk (GM) spectrum to define the characteristic frequency and wavenumber continuum of open-ocean internal waves. As the capabilities of instruments improved, scientists continued to uncover the importance of internal waves to both small- and large-scale physical processes (Figure 1; Garrett & Munk, 1979). This led to a branching of internal wave research, with recent studies focusing on important concepts such as internal wave generation and dissipation (Terker et al., 2014; Kunze, 2017), forcing response due to seasonal weather variability (Alford et al., 2012; Thomson & Krassovski, 2015), and the scattering and reflection of internal waves at slopes and canyons (Nash et al., 2004; Kunze et al., 2012; Gemmrich & Klymak, 2015).

Notable effects near irregular topography have highlighted these sites as drivers of internal wave activity. As internal waves and tides approach seamounts, slopes, or canyons, their energy is focused, cascading from low- to high-frequency processes, and eventually dissipate as heat (Garrett & Munk, 1979). This dissipation leads to an energetic local environment, evident as turbulent processes on the micro- (less than 1 m vertical) and fine-scales (1 m to 100 m vertical) (Garrett & Munk, 1979; Kunze et al., 2012). This then contributes to regional transport of energy and momentum, and the mixing of heat, pollutants, and biological constituents (Kunze et al., 2012). Furthermore, internal waves help to set ocean stratification, layers that drive large-scale systems such as the overturning circulation (Garrett & Munk, 1979). As such, understanding internal wave interactions with topography is important for predicting changes

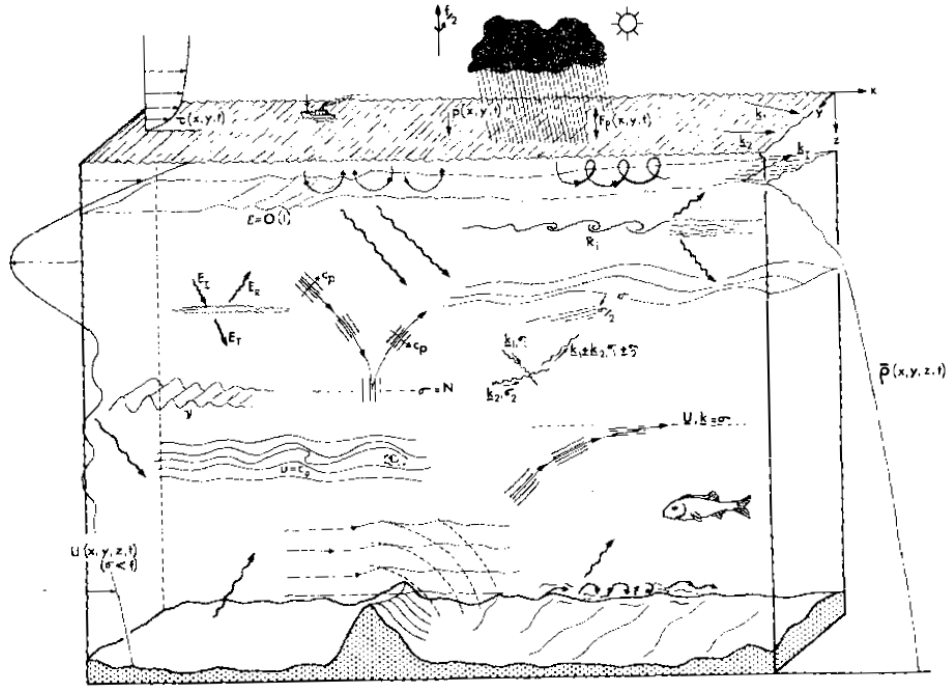


Figure 1: Generalised depiction of internal wave processes in the ocean, as envisioned by Garrett and Munk (1979).

in the coupled ocean-atmosphere climate system (Garrett & Munk, 1979).

Topography focused internal wave studies are numerous, and have been ongoing at locations such as the Hawaiian ridge (Alford et al., 2007), the slopes of the South China Sea (Klymak et al., 2011), and in slope-incising canyons of the northeastern Pacific (Allen et al., 2001; Carter & Gregg, 2002; Kunze et al., 2012; Terker et al., 2014). Canyons and their adjacent slopes have been identified as hot spots of internal wave activity, that not only generate (Carter & Gregg, 2002), but also dissipate internal waves and tides (Allen et al., 2001; Kunze et al., 2002). Research at Monterey Canyon, alone, has produced results regarding the scattering and reflection of internal waves and tides on critical slopes (Figure 2; Kunze et al., 2012), the presence of internal-bores and near-bottom turbulent layers that drive mixing (Carter & Gregg, 2002; Kunze et al., 2002), and correlation between topography and increased dissipation and generation of internal waves and tides (Terker et al., 2014). These results, among others, each highlight internal waves interactions with topography as drivers of regional physical processes.

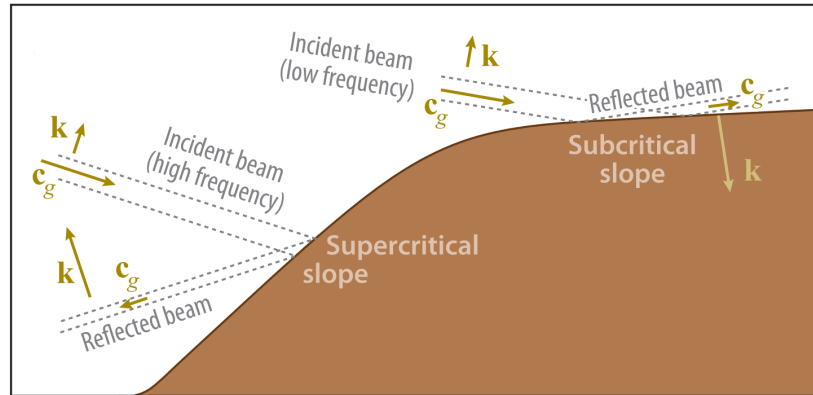


Figure 2: Graphic depiction of internal wave interactions with irregular topography. Adapted from Lamb (2014).

In Canada, research in the Pacific is often focused on the Vancouver Island Continental Shelf (VICS). Regional studies have led to results on seasonal wind forcing for near-inertial internal waves (Alford et al., 2012), potential evidence of non-linear wave-wave interaction between inertial internal waves and semidiurnal internal tides (Mihaly et al., 1998), locally generated coastal trapped waves (CTW) of diurnal frequency (Thomson & Crawford, 1982), and regional currents associated with the northeast Pacific current cycle (Thomson & Krassovski, 2015). The seasonally variable currents have been associated with observations of vorticity stretching and upwelling at the head of Barkley Canyon, suggesting considerable canyon influence on local water properties and transport of biological constituents (Allen et al., 2001); the VICS is one of the world's most productive shelf environments. As such, further research at Barkley Canyon is necessary to improve understanding of important regional mixing processes, and what drives them.

Despite considerable research into physical processes at the VICS, a better understanding of internal wave interactions at the bordering continental slope and its incising canyons is necessary for accurately predicting regional mixing contributions and resultant climate effects and biological productivity. As such, this research will evaluate horizontal velocity data from two sites, one in Barkley Canyon and another on the nearby slope, to provide information regarding regional mixing processes and their generation mechanics. This will include an analysis of seasonal variability in regional mean currents, tides, and winds, to identify forcing. Forcing will be correlated to observable internal wave events on the slope and within the canyon, and association expanded to

dissipative processes that may affect regional systems. Finally, the state of the internal wave continuum will be characterised through a comparison with accepted GM theory, to highlight topographic dependencies of the internal wave field.

3 Theory

Internal waves are dependent on stratification, but do not require a sharp density interface to exist; they are commonly found in continuously stratified fluids like the ocean interior, where density, $\rho(z)$, is a function of depth (z). The following is largely a concise adaptation of a much more detailed discussion by Kundu & Cohen (2008), cited here for clarity.

Stratification requires that internal wave theory consider buoyancy effects through depth. In order to describe the oscillatory motion of a fluid parcel displaced vertically, it is necessary to introduce the buoyancy frequency, N , as:

$$N^2 = -\frac{g}{\rho_0} \frac{\partial \rho(z)}{\partial z} \quad (1)$$

where g is the acceleration due to gravity, and ρ_0 is a reference density at a particular depth. Buoyancy effects allow for a consideration of wave propagation through a continuously stratified fluid, and suggests that internal waves are non-isotropic. Thus, for a 2D approximation, wavenumber (k and m), frequency (ω), and phase and group velocities (\mathbf{c}_p and \mathbf{c}_g) must be defined with vector qualities due to the importance of both magnitude and direction.

Furthermore, internal waves in a continuously stratified fluid are rotational processes. This further necessitates a derivation of a dispersion relation with appropriate buoyancy considerations and in vector form. However, as N varies with depth, this is a difficult task. If $N(z)$ is allowed to change with depth, vertical propagation of internal waves can be limited at 'turning depths'. The effect is better described by the Wentzel–Kramers–Brillouin (WKB) approximation, where for a single propagating wave ω and k are held fixed, while N is free to affect an adaptive vertical wavenumber, m (Garrett & Munk, 1979). For a simple model, however, it is found that the vertical change in N is slow enough, locally, that as a final leading assumption N can be considered depth independent.

Now, for a steady stratified flow with vertical velocity, w , where:

$$w = w_0 e^{i(kx + mz - \omega t)} \quad (2)$$

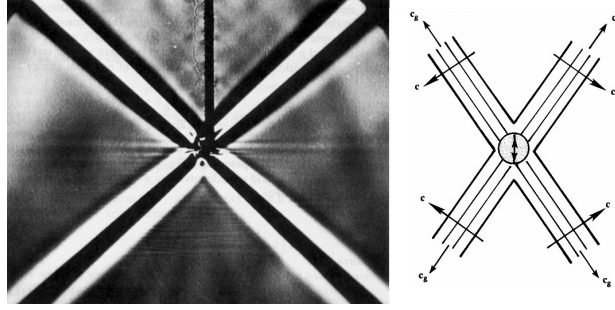


Figure 3: A photograph and graphic showing laboratory evidence for the symmetric radiation of 2D internal waves, from a source. Note the perpendicular phase and group velocities. Adapted from Kundu & Cohen (2008).

and w_0 is an amplitude, x the horizontal distance, and t is time, some algebraic work results in a surprisingly simple expression for the dispersion relation, where:

$$\omega = N \cos(\theta) \quad (3)$$

and θ is the angle from the x -axis to the direction of the phase velocity, \mathbf{c}_p . This suggests that not only does the frequency of internal waves only depend on the direction of the wavenumber (in θ), but that N is the limiting maximum frequency of internal waves. The maximum frequency of $\omega_{\max} = N$ is then found at the limit of $\theta = 0$, when the wavenumber is only horizontal, i.e. $m = 0$, so that the water column oscillates vertically. Furthermore, considering rotation effects, it is found that the limiting minimum frequency for internal waves, ω_{\min} , is the local Coriolis parameter, f (Garrett & Munk, 1979).

As a result of the directional dispersion relation, the group velocity, \mathbf{c}_g , is found to be perpendicular to the phase speed, \mathbf{c}_p ; i.e. their \mathbf{e}_1 components are the same, while their \mathbf{e}_3 components are opposite. This is interesting in that lines of phase propagate perpendicularly away from the beam of energy propagation associated with group velocity. It follows that in 2D, internal waves radiate group velocity outward from a source in four directions, each at an angle θ from vertical (Figure 3). This angle is defined by $\cos(\theta) = \omega/N$, with one beam in each quadrant, and phase radiating perpendicularly outward from each. From this result it follows that the energy flux per unit area is $\mathbf{F} = \mathbf{c}_g E$, where E is the energy per unit volume.

At this point, a discussion of internal waves mechanics can only continue by methodically eliminating governing assumptions. However, it is sufficient for the purposes of this paper to have provided a concise description of the fun-

damental theory. As a takeaway simplification, internal waves are sub-surface waves that propagate with perpendicular phase and group velocities outward from a source, exist due to density gradients in a fluid, and are contributors to significant physical processes such as large-scale mixing and transport.

4 Data

The obtained dataset is unique for both temporal and spatial consideration. Located at approximately 48.33°N 126.03°W, Barkley Canyon is about 75 km southwest of Vancouver Island, incising the continental slope and shelf with a rim and axis at depths of approximately -200 and -1000 m, respectively (Figure 4; Barkley Canyon, 2013). Spread along the topography of the canyon, Acoustic Doppler Current Profilers (ADCP) provide current data for Ocean Networks Canada (ONC), which maintains an array of instruments as part of the extensive NEPTUNE cabled observatory (ONC, 2013). ADCP emit acoustic beams that triangulate Doppler shifts in the water column, providing directional velocity data through time. For the selected instruments, the available time series is over ten years, much longer than is typically available for internal wave research, allowing for analysis of both seasonal and multi-annual trends. Furthermore, the broad placement of ADCPs, both in the canyon and on the nearby slope, allows for a comparative spatial analysis of internal wave effects at varied topography; a typically difficult prospect with single instruments or dropped observations.

For Barkley Canyon, the ONC Oceans 2.0 data portal offers publicly available data spanning over 10 years, from 2009 to present, at a sampling rate of as low as 2-seconds, depending on the instrument. The ADCP and their data are maintained, configured, and cleaned for distribution by ONC. Relevant ADCP were chosen at the Axis (75 and 55 kHz) and Upper Slope (75 kHz) sites. The Upper Slope 75 kHz ADCP sits below the VICS shelf-break at a depth of -378 metres (Figure 5), 75 km SW from Vancouver Island and 15 km NW of Barkley Canyon. The Axis 75 & 55 kHz ADCPs are located on the bottom of Barkley Canyon at a depth of -968 metres (Figure 5), about mid-length along the canyon at a sharp bend where a narrow north-south channel runs between adjacent outcrops to the east and west. Vertical resolution is 8 m depth bins for the 75 kHz instruments, and 20 m depth bins for the 55 kHz instrument.

To assess data quality and coverage, an initial quality check (error velocity, correlation, and backscatter intensity for both depth and time, based on ONC deployment parameters) was performed with raw 2-second and averaged 1-hour data. Afterwards, complete datasets for Upper Slope and Axis were

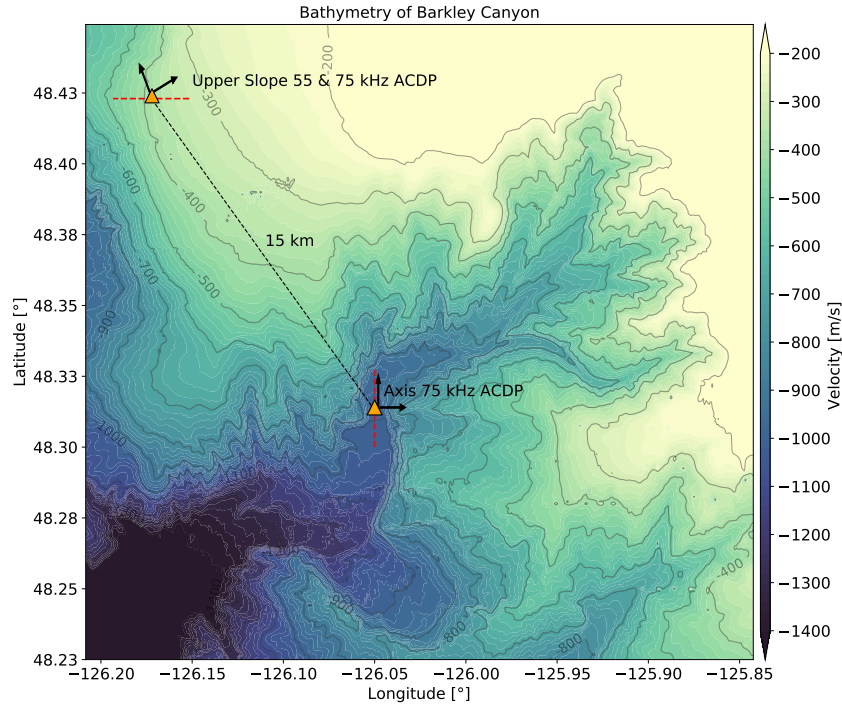


Figure 4: Bathymetry of Barkley Canyon. 3-arc-second mean sea level depth data obtained from the NOAA National Centre for Environmental Information. Perpendicular arrows at each site show rotated Cartesian coordinate systems, and the dashed red lines show the 3 km bathymetry cross-sections used for determining slope values for section 5.6 (cite).

downloaded in NetCDF format at a resolution of 15-minutes, determined to be adequate averaging of the data required for the science objectives of this research. Overlapping coverage of good quality (e.g. minimal gaps) is primarily during 2013, 2014, 2017, and 2018, and these years were chosen to provide the bulk of the multi-annual analysis, while 2013 will be used as the optimal reference year. Certain comparisons will be possible for other years and seasons, and made when necessary.

For preliminary data management, datasets were combined in their native NetCDF format, per instrument, and mapped to standard depth bins for ease of analysis. They were then depth-truncated to remove noise at the extreme depth limits of each instrument, determined from the initial quality checks, resulting in vertical extrema of -99 to -355 m for Upper Slope data, and -693 to -914 m for Axis data. NaN values were interpolated using a linear process

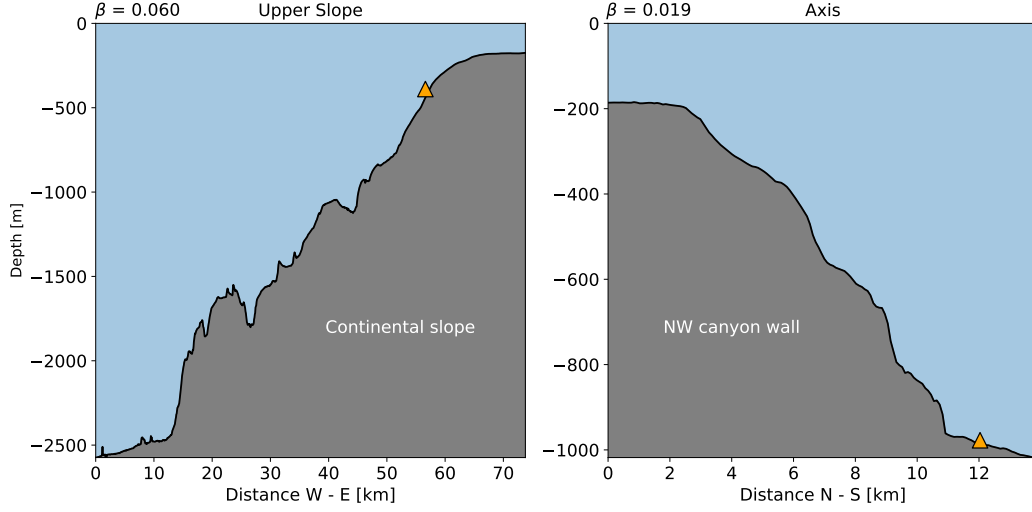


Figure 5: Site topography. Local site topography showing the relative location for Upper Slope (left) and Axis (right) instruments. Horizontal cross-sections were taken in the W-E (left) and N-S (right) directions. Horizontal distances range from the shelf to the abyssal plain (left) and canyon floor (right) (cite).

for gaps less than a day. To deal with larger data gaps, the datasets were subdivided within the NetCDF file and labelled by year and section, then combined using a weighted average as needed. At Upper Slope, data were rotated using a standard rotation matrix as:

$$u_{rot} = u \cos(\theta) - v \sin(\theta) \quad (4)$$

$$v_{rot} = u \sin(\theta) + v \cos(\theta) \quad (5)$$

where θ is the rotation angle in radians. This was done to better match the cross-slope angle of approximately $+30^\circ$, to help identify relationships between the predominant VICS currents and local slope topography; u is referred to as 'cross-slope', and v is 'along-slope' (Figure 4). At the Axis site, the along-canyon (v) direction is approximately north-south, so no rotation was necessary; u is referred to as cross-canyon.

Supplementary data were obtained from secondary sources as needed. Instrument baseline operational parameters were obtained from Nortek and Teledyne product datasheets. Bathymetry data were obtained from the National Oceanic and Atmospheric Administration (NOAA) National Centre for Environmental Information, as 3 arc-second resolution mean sea level depth. Wind data were obtained from the closest Fisheries and Oceans Canada (DFO)

weather buoy, Neah Bay (46206), as a time series of magnitude and direction for the comparison years. Conductivity-temperature-depth (CTD) climatology data were obtained from the nearby Station LB14, sampled annually May and September during DFO operated La Perouse research cruises, with casts down to -1180 m. Surface-level data were obtained from the Canadian Hydrographic Service (CHS) operated gauge in Tofino, nearly directly north of Barkley Canyon, as a time series of deviation from chart datum, in February 2013.

5 Methods

5.1 Velocities

Simple time - depth velocity plots can highlight both temporal and spacial trends in the data (Figure 6). To identify differences in the time domain of mean currents and tides, and to show seasonality and depth-dependence, a 40-hour, 8th-order, digital low-pass Butterworth filter was applied to the horizontal velocity data, and the resulting low-pass and residual data examined. Similar band-pass filters were applied to highlight current trends for specific frequency bands.

Additionally, high temporal-resolution wind data were smoothed using a vector process for both direction and magnitude, to compare with seasonal trends and identify forcing in both velocity and spectrogram analyses.

5.2 Power spectral density

To observe the relative frequency domain strength of specific constituents or bands, power spectra are useful tools (Figure 7). To determine power spectral density (PSD), the mean was first removed for each depth bin of unfiltered data. A Welch method one-sided Fast Fourier Transform (FFT) spectrogram process was performed at each depth, with a Hanning window and averaging parameters of 1024 data points per segment, and a 50% overlap. This supplied an output matrix of time (5.3-day intervals), depth, and frequency, which could be averaged for longer intervals. 95% confidence intervals were calculated using a χ^2 method.

To show the limitations of instrument sampling, the noise floor is the effective lower limit of an instrument for detecting measurement fluctuations, due to inherent noise in the electrical system. In spectral analysis, the noise floor can be thought of as the upper power limit of the inherent noise spectrum, which is equal throughout the frequency domain. To calculate, the standard deviation of the instrument sampling can be applied per ping, adjusted as necessary

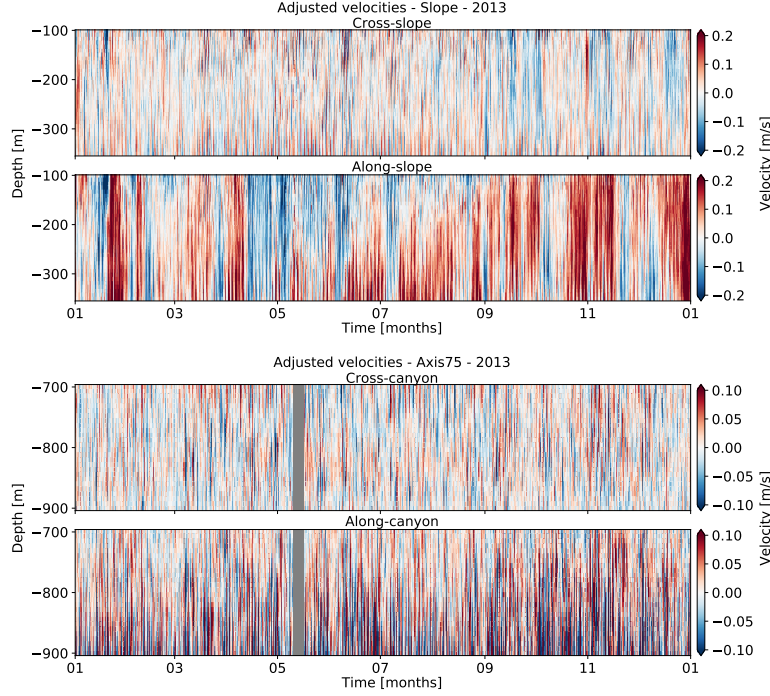


Figure 6: Unfiltered horizontal velocity data for Upper Slope (top) and Axis (bottom) in 2013. For each, components are separated as cross- (upper) and along-slope (lower). Velocities are 'adjusted', in that they have been rotated and NaN-interpolated, as detailed in section 5.1. Intensity has been scaled for clear visual representation of trends.

for time-averaged sampling intervals (through standard error of the mean), to determine the total noise variance. This is then applied to the rearranged integral of the noise spectrum, as noise floor level = total noise variance / bandwidth.

Additionally, climatology data were used to determine regional water properties, leading to stratification factors through depth. From the CTD data, depth-dependent values were obtained for temperature (T), pressure (P), and salinity (S). These were used to obtain potential temperature (θ), and potential density (ρ_θ) using the UNESCO 1983 (EOS 80) polynomial. The depth-dependent buoyancy frequency was then determined as in Equation 1. To deal with the effects of evident stratification, a smoothed depth-dependent

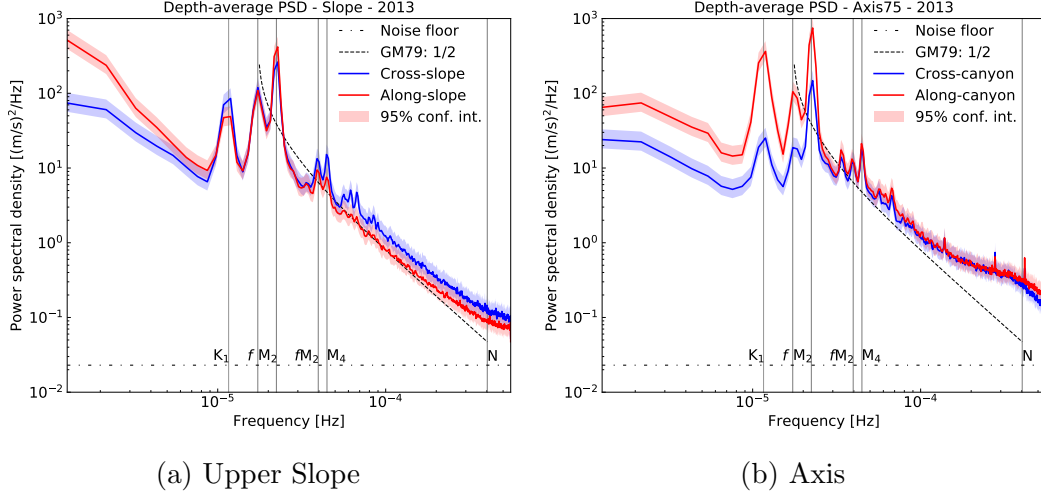


Figure 7: Annual time- and depth-averaged PSD for (a) Upper Slope and (b) Axis in 2013, from adjusted horizontal velocity data. Both cross- (blue) and along-slope (red) components are shown for comparison, with 95% confidence intervals. For reference, the instrument noise floor (dotted line), component-wise GM79 spectrum (dashed line), and key frequency constituents (vertical lines) are shown.

WKB-scaling factor was determined as:

$$z_{WKB} = \frac{1}{N_0} \int_0^z N(z) dz \quad (6)$$

with a reference buoyancy frequency of $N_0 = 2.53 \times 10^{-3}$ rad/s based on a reference depth averaged around -904 m, the lowest evaluated. This WKB-stretch scaling factor was applied for each depth bin, to mitigate stratification effects at the pycnocline, etc.

Regional water properties were further used to determine the local GM internal wave spectrum as it would appear for the open ocean, for comparison with observed spectra. The process was adapted from Callies (2016), using local parameters $f = 1.73 \times 10^{-5}$ Hz, $g = 9.81(m/s)^2$, and N_0 , along with canonical values for the surface-extrapolated buoyancy frequency (5.24×10^{-3} rad/s), e-folding scale of $N(z)$ (1.3×10^3 m), mode scale number $j^* = 3$, and dimensionless internal wave energy parameter $E = 6.3 \times 10^{-5}$, following from Munk's seminal chapter in Wunsch's *Evolution of Physical Oceanography* (1981).

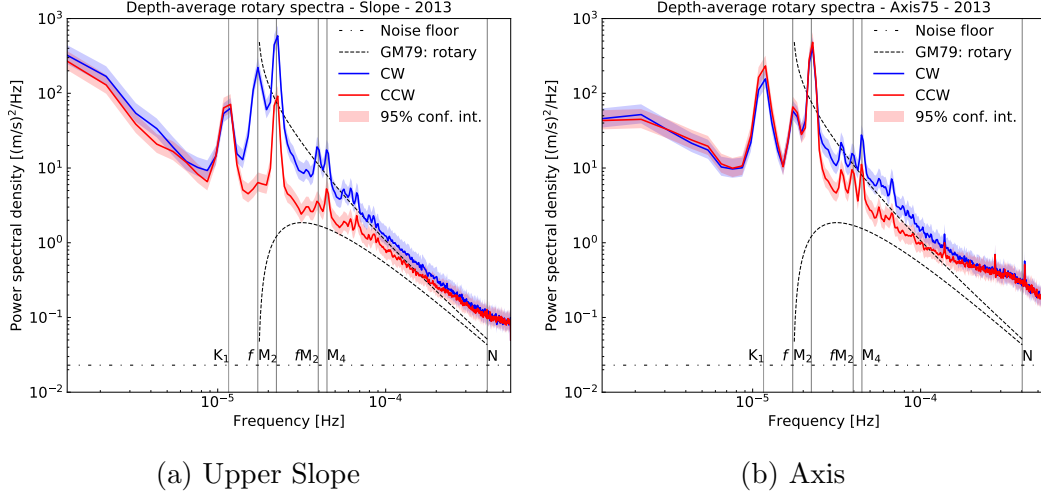


Figure 8: Annual time- and depth-averaged rotary spectra for (a) Upper Slope and (b) Axis in 2013, from adjusted horizontal velocity data. Both CW (blue) and CCW (red) components are shown for comparison, with 95% confidence intervals. For reference, the instrument noise floor (dotted line), rotary GM79 spectrum (dashed lines), and key frequency constituents (vertical lines) are shown.

5.3 Rotary spectra

To better interpret rotation effects, rotary spectra were developed using similar parameters as for PSD, with a more involved spectrogram FFT process based on the work of Gonella (1972), and Thomson and Emery (2014) (Figure 8). To summarise, the adjustment to find the counter-clockwise (CCW) and clockwise (CW) components of a complex horizontal velocity vector, $\mathbf{w}(t) = u(t) + iv(t)$, is the addition or subtraction of the quadrature spectrum, Q_{uv} , as:

$$\text{CCW} = \frac{1}{2}[S_{uu} + S_{vv} + 2Q_{uv}] \quad (7)$$

$$\text{CW} = \frac{1}{2}[S_{uu} + S_{vv} - 2Q_{uv}] \quad (8)$$

where S_{uu} and S_{vv} are the typical complex autospectra used to determine PSD (Thomson & Emery, 2014).

The standard GM spectrum obtained for comparison with PSD was also adapted for rotary spectra. Application of the rotary consistency relation:

$$\frac{\text{CCW}}{\text{CW}} = \frac{(\omega - f)^2}{(\omega + f)^2} \quad (9)$$

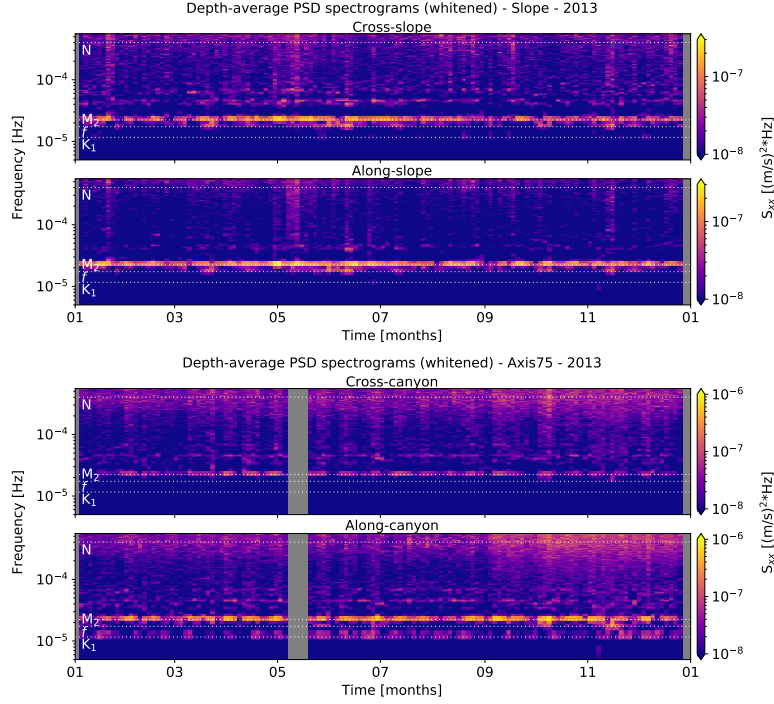


Figure 9: Annual PSD spectrograms for Upper Slope (top) and Axis (bottom) in 2013, from adjusted horizontal velocity data. For each, both cross- (upper) and along-slope (lower) components are shown for comparison, with 95% confidence intervals. For reference, key frequency constituents (horizontal lines) are shown. Spectrograms are 'whitened' (see section 5.4) and intensity has been scaled for clear visual representation of trends.

to the GM kinetic energy spectrum results in rotary adjusted spectra for both CCW and CW components (Levine, 2002; Polzin & Lvov, 2011).

5.4 Spectrograms

For analysis of frequency domain seasonality, spectrograms are a common tool. However, the PSD and rotary spectrograms described were taken specifically for averaging into those formats, with appropriate resolution to resolve plotted spectral peaks. With the intent of observing seasonality, a similar spectrogram FFT process was performed with a window of only 512 data points per segment, resulting in a better temporal resolution of 2.7-day intervals. These were created in both Cartesian (Figure 9) and rotary (Figure 10) formats. Spectrograms were 'whitened' by multiplying each power bin by its respective frequency, squared, to better show continuum seasonality.

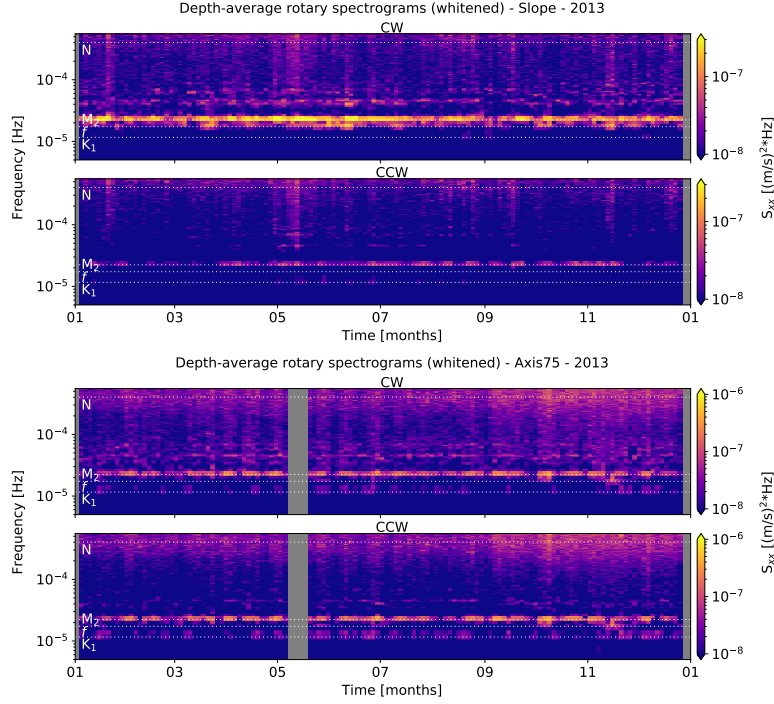


Figure 10: Annual rotary spectrograms for Upper Slope (top) and Axis (bottom) in 2013, from adjusted horizontal velocity data. For each, both cross-slope (upper) and along-slope (lower) components are shown for comparison, with 95% confidence intervals. For reference, key frequency constituents (horizontal lines) are shown. Spectrograms are 'whitened' (see section 5.4) and intensity has been scaled for clear visual representation of trends.

5.5 Depth-band integrated power

The seasonality-focused spectrogram data were further inspected for depth-dependence of PSD and rotary indicated primary frequency constituents. Each frequency band was integrated over a bandwidth estimated to encompass the majority of the respective spectral peak or continuum. This was performed for each depth bin along consecutive time steps. The output results in 'depth-band integrated power' spectrograms, useful for inspecting a specific frequency band's depth relationship with local topography.

Depth-band integrated power also highlights seasonality for each band. As such, comparisons with mean currents, wind, and barotropic tides were performed. Barotropic tidal data were obtained from sea-surface level measurements, and their power spectra band-pass filtered to compare with the

depth-mean component of the depth-band integrated power spectrograms, for a spring-neap phase comparison to estimate the locality of tidal forcing.

5.6 Critical slope analysis

For observations of free internal waves and tides incident with sloping topography (continental slope, canyon axis and walls, etc.), the angle of the incident wave, α , and the approximate rise of the topography, β , have a direct relationship. The incident internal wave angle of propagation is evaluated through Equation 10, as:

$$\alpha = \sqrt{\frac{(\omega^2 - f^2)}{(N^2 - \omega^2)}} \quad (10)$$

where ω is the incident wave frequency. To generalise, for $\beta > \alpha$, the slope is considered supercritical and incident waves are reflected back to the open ocean depths; for $\beta \approx \alpha$, the slope is considered critical and the incident waves are amplified; and for $\beta < \alpha$, the slope is considered subcritical and incident waves are scattered up-slope.

For the Upper Slope site, the critical slope angle was determined from rise-over-run estimates along a 3 km E-W bathymetry cross-section centred at the ADCP site (Figures 4 and 5), to be $\beta \approx 0.060$, leading to a critical frequency of $\omega_c = 3 \times 10^{-5}$ Hz. This portion of the continental slope is therefore supercritical (reflective) to internal waves and tides with frequencies below ω_c .

For the Axis site canyon floor (along-canyon slope), the critical slope angle was determined from rise-over-run estimates along a 3 km N-S bathymetry cross-section centred at the ADCP site (Figures 4 and 5), to be $\beta \approx 0.019$, leading to a critical frequency that is sub-inertial. As such, this portion of the canyon floor is subcritical to all freely propagating internal waves and tides, and should scatter incident waves up-canyon.

The Axis site canyon walls are difficult to quantify in terms of β , due to highly variable topography, but in general are moderately steep and supercritical to even the semidiurnal constituent. This will be a leading assumption in section 6.3, below.

Finally, regions of near-criticality, where $\beta/\alpha \approx 1$, have been found to intensify incident waves of near-critical frequency, despite reflection or scattering processes that may still occur.

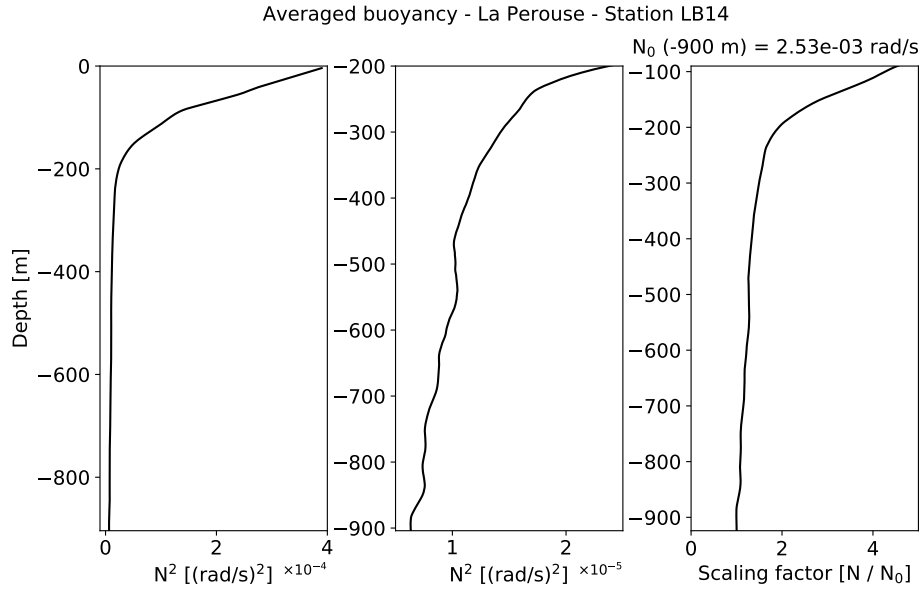


Figure 11: Averaged N^2 parameter and WKB-stretch scaling factor. Buoyancy results were obtained as detailed in section 5.2, and are displayed through the water column (left) and below -200 m (centre). A WKB-stretch scaling factor (right) was determined as in Equation 6, based on N_0 .

6 Results

6.1 Seasonality

Move outline here.

Figure: Multi-annual spectrograms, each site

Figure: Wind vs velocity vs reference spectrogram

Figure: Spring-neap vs spectrogram

6.2 Slope effects

In addition to the seasonal effects noted in section 6.1, the depth dependence of each frequency band is notably affected by proximity to topography. For Upper Slope, this is evident in changes to direction (Figure 12) and rotation (Figure 13), and the intensification of a thick (~ 150 m) layer directly above the bottom (Figures 12 and 13). The instrument location below the VICS shelf-break (Figure 5), at a depth of -378 m, suggests that this depth dependence is related to the effects of the supercritical upper continental slope on incident and locally generated internal waves and tides.

First, in the upper depths (above -250 m), there appears to be little influence from the slope. All bands experience prominently CW motions, as expected due to rotation effects in the northern hemisphere. Furthermore, all bands experience close to equal distribution between cross- and along-slope directionality. When observing non-WKB-stretch scaled spectra, there is obvious near-surface intensification above the pycnocline. The WKB-stretch scaling largely removes this effect, so a connection to stratification is obvious. However, the WKB-stretch scaling is based on deep CTD casts that were made nearby, but away from topography; the stratification profile captures the surface mixed-layer, but does not adjust for possible stratification effects near the slope (Figure 11). Hotchkiss and Wunsch (1982) noted increased stratification effects near areas of high 'topographic relief', such as the shelf-break and slopes. These highly stratified turbulent layers experience the effects of reflection, scattering, and internal tide and lee-wave generation, as well as amplification of internal waves and tides, in general.

It is below -250 m where slope effects arise and increase with proximity to the bottom. All bands, excluding the near-inertial, show a near-slope intensification of $1\times$ to over $2\times$ orders of magnitude; the near-inertial band shows little sign of this intensification. The subdiurnal and diurnal bands show strong intensification in the CCW rotary component (about $1.5\times$ orders of magnitude), suggesting upward propagation or reflection from the slope. The semidiurnal (about $2\times$ orders of magnitude) and continuum (about $1\times$ orders of magnitude) bands show CW intensification, suggesting downward propagation or reflection. The subdiurnal and diurnal intensification is mostly in the along-slope direction, while the semidiurnal and continuum bands both see a close to equal distribution between the cross- and along-slope components, as they are distributed in the upper depths. Furthermore, both the diurnal and near-inertial bands show a CW weakening with proximity to the slope. The other bands show no weakening effects; their intensified components simply rise to meet or overtake those dominant in the upper depths. All bands are affected

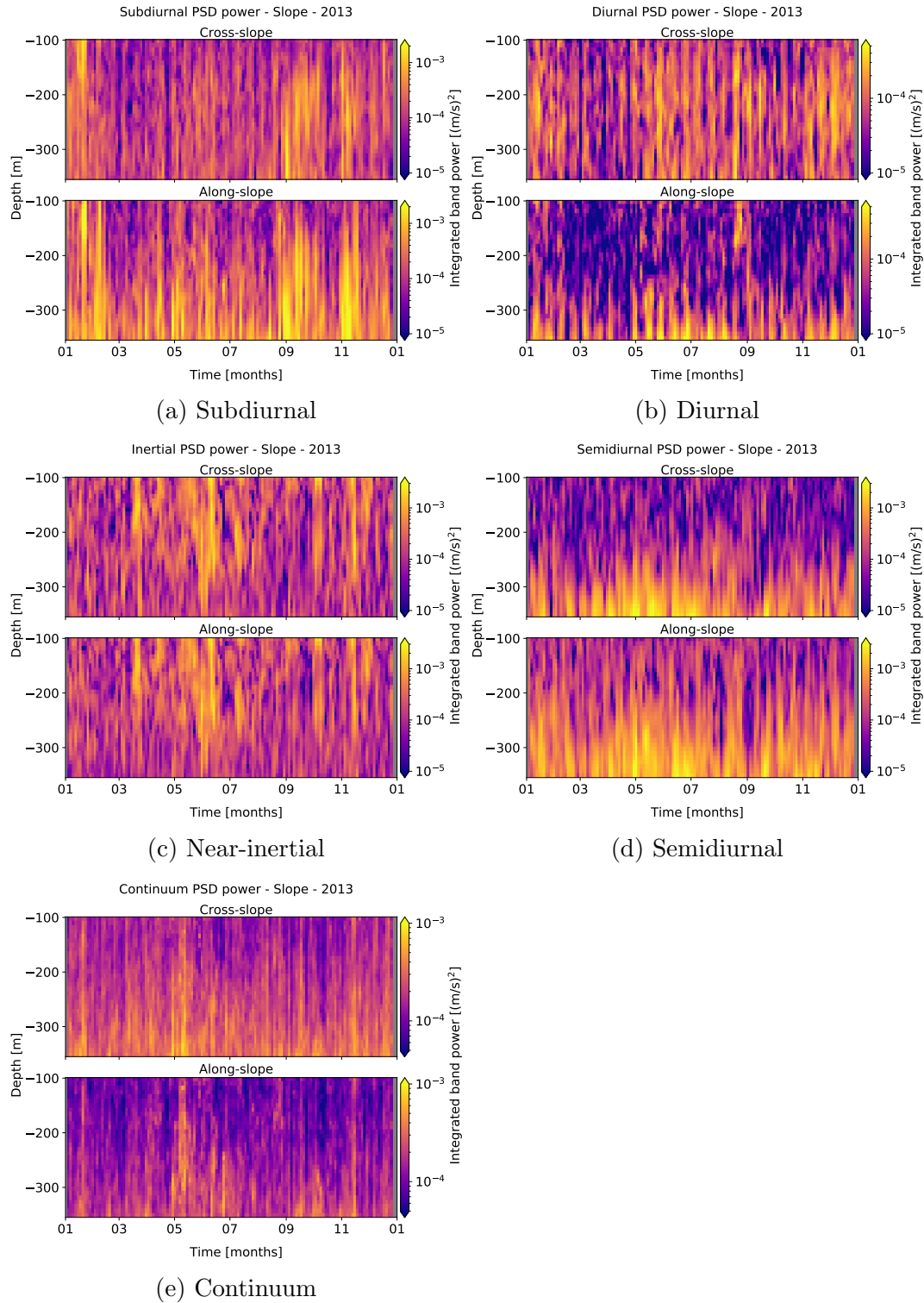


Figure 12: Band-integrated PSD data for Upper Slope in 2013, for rotated, cleaned, and WKB-scaled horizontal velocity data. For each sub-figure, there are cross- (top) and along-slope (bottom) components. Intensity scales are adjusted for visual clarity of effects.

over a similar vertical scale of approximately 150 m above bottom (AB), up to 200 m AB in certain instances.

Continental slopes are common study sites, and their non-uniform geometry is known to have significant effects on both incident and locally generated internal waves and tides. Intensified near-slope layers are prevalent in the literature, noted in similar cases by Kunze et al. (2012), Nash et al. (2004), and Polzin et al. (1997). Similar results are traceable back to a seminal study by Hotchkiss and Wunsch, in 1982, who found a $\sim 10\times$ increase in near-slope internal wave energy near Hudson Canyon, with a depth-dependent vertical scale of about 150 m AB at -400 m depth. More recently, Robertson et al. (2017) found that where criticality (β/α , as detailed in section 5.6) is near to 1, typically below the shelf-break and along the upper slope, diurnal and semidiurnal internal tides were most strongly subject to near-slope enhancement. Xie and Chen (2021) found further evidence of near-critical bottom-enhancement of diurnal and semidiurnal internal tides exceeding 150 m AB, in the South China Sea.

For Barkley Canyon and the nearby slope, the diurnal constituent is sub-inertial, so it is unlikely for there to be incident diurnal internal tides from the open ocean. At slopes along the California Current System, Johnston and Rudnick (2015) found that generated sub-inertial diurnal internal tides were evanescent (trapped) to slope topography poleward of their turning latitude ($\sim 30^\circ\text{N}$), but could still propagate alongshore. Robertson et al. (2017) found further evidence of trapped diurnal internal tides at Barcoo seamount, north of their turning latitude, where generated diurnal currents were strong along-slope but could not propagate away from the supercritical topography. At Barkley Canyon, the 'rubbing' of the barotropic diurnal tide along the slope should still produce diurnal internal tides; however, these would be trapped radiating upward (CCW) near to the topography in a concentrated layer, only able to really propagate in the along-slope direction, as observed. Additionally, poleward propagation of free baroclinic CTW of diurnal frequency from the mouth of the nearby Strait of Juan de Fuca may contribute to the observed along-slope currents, though this is debatable as their strength should diminish with depth beyond the shelf-break (Thomson et al., 1982; Kuroda et al., 2018). These same effects could also apply to the subdiurnal band, being similarly sub-inertial, with forcing at such low frequencies possibly being due to regional mean currents.

For near-inertial internal waves, which are generated by wind at the ocean surface and propagate downward, Thomson et al. (1990) found that as they approach a slope they become somewhat attenuated as they are absorbed by increased vertical shear in the background flow, due to topographically

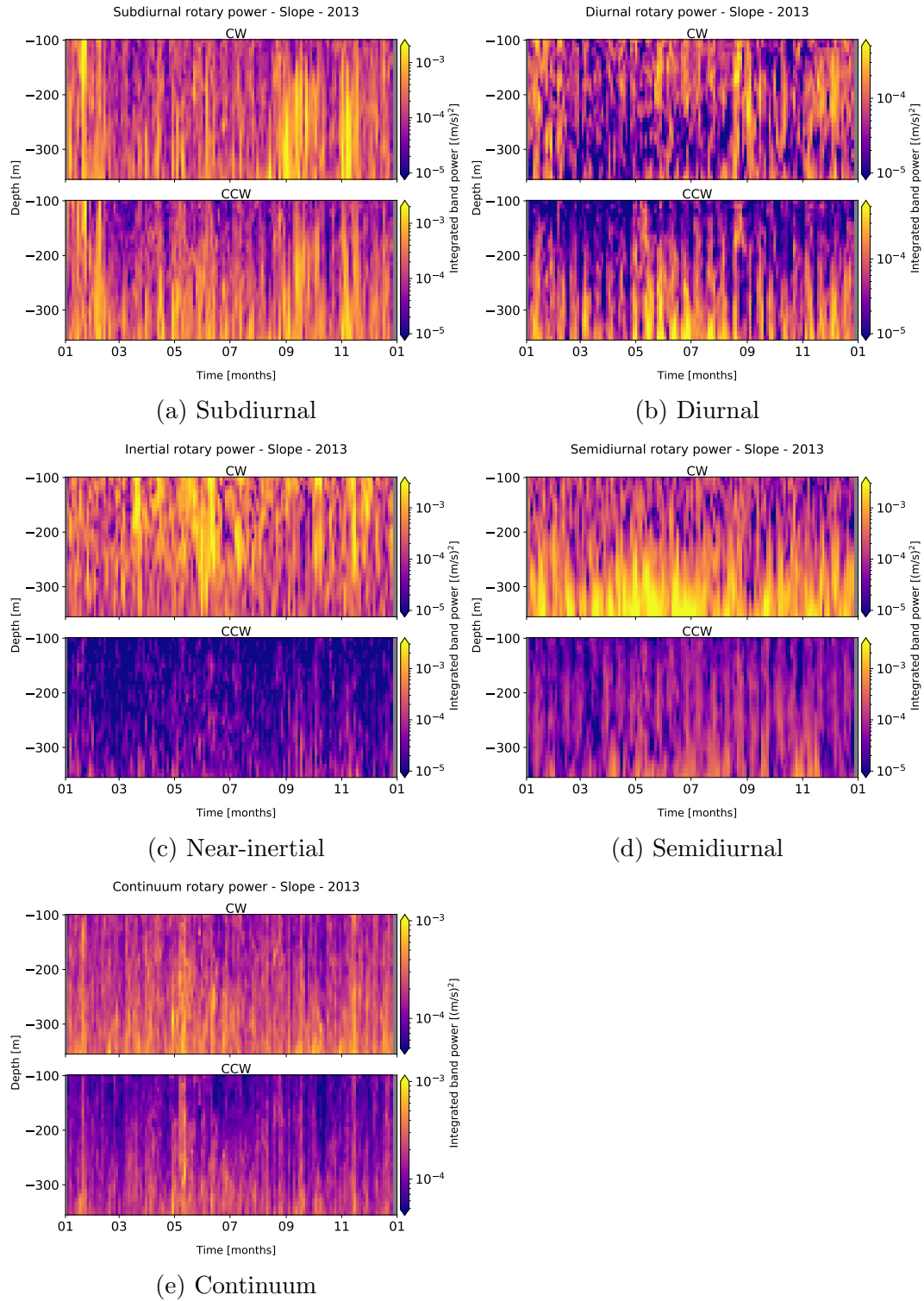


Figure 13: Band-integrated rotary data for Upper Slope in 2013, for rotated, cleaned, and WKB-scaled horizontal velocity data. For each sub-figure, there are CW (top) and CCW (bottom) components. Intensity scales are adjusted for visual clarity of effects.

trapped oscillations. Since the Upper Slope site is supercritical ($\beta \approx 0.060$) to near-inertial frequencies ($\alpha \approx 0.023$), the CW reduction near-bottom is as expected. It is further possible that downward propagating near-inertial internal waves that are not entirely attenuated are then reflected downward, maintaining some presence in the lower layer. Furthermore, the intensification in this band should be minimal compared to what is observed for the semidiurnal constituent, consistent with a relatively weak near-inertial criticality parameter ($\beta/\alpha \approx 2.6$) at this site. Indeed, intensification in the near-inertial band is barely evident.

In terms of the semidiurnal band, Terker et al. (2014) found evidence of near-bottom elevated energy-flux associated with semidiurnal internal tide generation on the continental slope near Monterey Bay, with a vertical scale of about 200 m AB in similar depths to the Upper Slope site. Marques et al. (2020) found further evidence of bottom-enhanced semidiurnal energy at a supercritical slope near Tasmania, of up to $10\times$ intensification. Off the west coast of India, Subeesh et al. (2021) found that for sites offshore of the shelf-break generation zone, propagation for the baroclinic semidiurnal tide is downward; furthermore, the supercritical upper slope prevents much of the incident offshore semidiurnal internal tides from propagating onto the shelf, as they're reflected back to the open ocean, again downward. As the Upper Slope site is supercritical to the semidiurnal constituent ($\alpha \approx 0.037$), any incident semidiurnal internal tides should be reflected downward, as is suggested by the strong CW intensification observed. Additionally, a stronger criticality parameter ($\beta/\alpha \approx 1.6$) suggests amplification of semidiurnal waves to a much greater degree than for the near-inertial or continuum bands, also evident in the observations. Finally, Xie and Chen (2021) noted that for obliquely incident internal waves and tides, generated near-slope currents are in the direction of incident wave propagation; the semidiurnal intensified signal is nearly equally distributed between cross- and along-slope components, similar to its state in the upper depths.

Intensification in the super-tidal internal wave continuum is more subtle. As the band is broad, much of it is far from being near-critical, so intensification is weaker than for other constituents such as the semidiurnal, as expected. Although the background state of the band appears to trend slightly towards the cross-slope and CW components, intensification seems to apply somewhat equally to all components; everything intensifies by a factor of about $1\times$ order of magnitude. Besides the entirety of this band being less energetic than the tidal and near-inertial constituents, it is possible that the (relatively) small-scale motions characterised by these higher frequencies act to reduce the scale

of the near-slope effects. - Wunsch chapter 2 'critical layers' to finish this paragraph.

6.3 Canyon effects

Move outline here.

6.4 Continuum analysis

Move outline here.

Figure: Panels of power law fits to continuum.

7 Discussion

Expanded possible explanations and connections (where necessary)

Speculation

Sources of error and improvements

Potential for future research

Figure: Supplemental to Discussion

8 Conclusions

Summary of importance and goals (brief).

Summary of data and methods (brief).

Summary of findings and possible explanations (brief).

Summary of errors, improvements, and potential future research (brief).

Exciting final statement regarding findings.

9 References

- Alford, M. H., MacKinnon, J. A., Zhao, Z., Pinkel, R., Klymak, J., & Peacock, T. (2007). Internal waves across the Pacific. *Geophysical Research Letters*, 34(24), 24601. <https://doi.org/10.1029/2007GL031566>
- Alford, M. H., Cronin, M. F., & Klymak, J. M. (2012). Annual cycle and depth penetration of wind-generated near-inertial internal waves at ocean station papa in the northeast pacific. *Journal of Physical Oceanography*, 42(6), 889–909. <https://doi.org/10.1175/JPO-D-11-092.1>
- Allen, S. E., Vindeirinho, C., Thomson, R. E., Foreman, M. G. G., & Mackas, D. L. (2001). Physical and biological processes over a submarine canyon during an upwelling event. *Canadian Journal of Fisheries and Aquatic Sciences*, 58(4), 671–684. <https://doi.org/10.1139/f01-008>
- Carter, G. S., & Gregg, M. C. (2002). Intense, variable mixing near the head of Monterey Submarine Canyon. In *Journal of Physical Oceanography* (Vol. 32). [https://doi.org/10.1175/1520-0485\(2002\)032;3145:IVMNTH;2.0.CO;2](https://doi.org/10.1175/1520-0485(2002)032;3145:IVMNTH;2.0.CO;2)
- Crawford, W. R., & Thomson, R. E. (1984). Diurnal-Period Continental Shelf Waves along Vancouver Island: A Comparison of Observations with Theoretical Models. *Journal of Physical Oceanography*, 14(10), 1629–1646. [https://doi.org/10.1175/1520-0485\(1984\)014;1629:dpcswa;2.0.co;2](https://doi.org/10.1175/1520-0485(1984)014;1629:dpcswa;2.0.co;2)
- Cummins, P. F., Masson, D., & Foreman, M. G. G. (2000). Stratification and mean flow effects on diurnal tidal currents off Vancouver Island. *Journal of Physical Oceanography*, 30(1), 15–30. [https://doi.org/10.1175/1520-0485\(2000\)030;0015:SAMFEO;2.0.CO;2](https://doi.org/10.1175/1520-0485(2000)030;0015:SAMFEO;2.0.CO;2)
- Garrett, C., & Munk, W. (1979). Internal Waves in the Ocean. In *Ann. Rev. Fluid Mech* (Vol. 11).
- Gemmrich, J., & Klymak, J. M. (2015). Dissipation of internal wave energy generated on a critical slope. *Journal of Physical Oceanography*, 45(9), 2221–2238. <https://doi.org/10.1175/JPO-D-14-0236.1>
- Gonella, J. (1972). A rotary-component method for analysing meteorological and oceanographic vector time series (Vol. 19). Pergamon Press.
- Hendershott, M. C., & Garrett, C. (2018). Internal Tides. In *Geophysical Fluid Dynamics* (No. 6). Retrieved from <https://gfd.whoi.edu/wp-content/uploads/sites/18/2018/03/lecture0621>
- Hotchkiss, F. S., & Wunsch, C. (1982). Internal waves in Hudson Canyon with

- possible geological implications. *Deep Sea Research Part A, Oceanographic Research Papers*, 29(4), 415–442. [https://doi.org/10.1016/0198-0149\(82\)90068-1](https://doi.org/10.1016/0198-0149(82)90068-1)
- Johnston, T. M. S., & Rudnick, D. L. (2015). Trapped diurnal internal tides, propagating semidiurnal internal tides, and mixing estimates in the California Current System from sustained glider observations, 2006-2012. *Deep-Sea Research Part II: Topical Studies in Oceanography*, 112, 61–78. <https://doi.org/10.1016/j.dsr2.2014.03.009>
- Klymak, J. M., Alford, M. H., Pinkel, R., Lien, R. C., Yang, Y. J., & Tang, T. Y. (2011). The breaking and scattering of the internal tide on a continental slope. *Journal of Physical Oceanography*, 41(5), 926–945. <https://doi.org/10.1175/2010JPO4500.1>
- Kundu, P. K., & Cohen, I. (2008). *Fluid mechanics*. (4th ed.). Academic Press.
- Kunze, E. (2017). Internal-wave-driven mixing: Global geography and budgets. *Journal of Physical Oceanography*, 47(6), 1325–1345. <https://doi.org/10.1175/JPO-D-16-0141.1>
- Kunze, E., Rosenfeld, L. K., Carter, G. S., & Gregg, M. C. (2002). Internal waves in Monterey Submarine Canyon. *Journal of Physical Oceanography*, 32(6), 1890–1913. [https://doi.org/10.1175/1520-0485\(2002\)032;1890:IWIMSC;2.0.CO;2](https://doi.org/10.1175/1520-0485(2002)032;1890:IWIMSC;2.0.CO;2)
- Kunze, E., Mackay, C., Mcphee-Shaw, E. E., Morrice, K., Girton, J. B., & Terker, S. R. (2012). Turbulent mixing and exchange with interior waters on sloping boundaries. *Journal of Physical Oceanography*, 42(6), 910–927. <https://doi.org/10.1175/JPO-D-11-075.1>
- Kuroda, H., Kusaka, A., Isoda, Y., Honda, S., Ito, S., & Onitsuka, T. (2018). Diurnal tidal currents attributed to free baroclinic coastal-trapped waves on the Pacific shelf off the southeastern coast of Hokkaido, Japan. *Continental Shelf Research*, 158, 45–56. <https://doi.org/10.1016/j.csr.2018.02.010>
- Lamb, K. G. (2014). Internal wave breaking and dissipation mechanisms on the continental slope/shelf. *Annual Review of Fluid Mechanics*, 46, 231–254. <https://doi.org/10.1146/annurev-fluid-011212-140701>
- Levine, M. D. (2002). A modification of the Garrett-Munk internal wave spectrum. *Journal of Physical Oceanography*, 32(11), 3166–3181. [https://doi.org/10.1175/1520-0485\(2002\)032;3166:AMOTGM;2.0.CO;2](https://doi.org/10.1175/1520-0485(2002)032;3166:AMOTGM;2.0.CO;2)

- Marques, O. B., Alford, M. H., Pinkel, R., MacKinnon, J. A., Klymak, J. M., Nash, J. D., ... Braznikov, D. (2020). Internal Tide Structure and Temporal Variability on the Reflective Continental Slope of South-eastern Tasmania. *Journal of Physical Oceanography*, 51(2), 611–631. <https://doi.org/10.1175/jpo-d-20-0044.1>
- Martini, K. I., Alford, M. H., Kunze, E., Kelly, S. M., & Nash, J. D. (2013). Internal bores and breaking internal tides on the Oregon continental slope. *Journal of Physical Oceanography*, 43(1), 120–139. <https://doi.org/10.1175/JPO-D-12-030.1>
- Mihaly, S. F., Thomson, R. E., & Rabinovich, A. B. (1998). Evidence for non-linear interaction between internal waves of inertial and semidiurnal frequency. *Geophysical Research Letters*, 25(8), 1205–1208. <https://doi.org/10.1029/98GL00722>
- Munk, W., & Garrett, C. (1979). Internal Waves and Small-Scale Processes. In C. Wunsch (Ed.), *Evolution of Physical Oceanography*.
- Nash, J. D., Kunze, E., Toole, J. M., & Schmitt, R. W. (2004). Internal tide reflection and turbulent mixing on the continental slope. In *Journal of Physical Oceanography* (Vol. 34). [https://doi.org/10.1175/1520-0485\(2004\)034;1117:ITRATMj2.0.CO;2](https://doi.org/10.1175/1520-0485(2004)034;1117:ITRATMj2.0.CO;2)
- Polzin, K. L., & Lvov, Y. V. (2011). Toward regional characterizations of the oceanic internal wavefield. *Reviews of Geophysics*, 49(4), 4003. <https://doi.org/10.1029/2010RG000329>
- Robertson, R., Dong, J., & Hartlipp, P. (2017). Diurnal Critical Latitude and the Latitude Dependence of Internal Tides, Internal Waves, and Mixing Based on Barcoo Seamount. *Journal of Geophysical Research: Oceans*, 122(10), 7838–7866. <https://doi.org/10.1002/2016JC012591>
- Subeesh, M. P., Unnikrishnan, A. S., & Francis, P. A. (2021). Generation, propagation and dissipation of internal tides on the continental shelf and slope off the west coast of India. *Continental Shelf Research*, 214. <https://doi.org/10.1016/j.csr.2020.104321>
- Terker, S. R., Girton, J. B., Kunze, E., Klymak, J. M., & Pinkel, R. (2014). Observations of the internal tide on the California continental margin near Monterey Bay. *Continental Shelf Research*, 82, 60–71. <https://doi.org/10.1016/j.csr.2014.01.017>
- Thomson, R. E., & Crawford, W. R. (1982). The Generation of Diurnal Period Shelf Waves by Tidal Currents in: *Journal of Physical Oceanography*

- Volume 12 Issue 7 (1982). *Journal of Physical Oceanography*, 12(7).
- Thomson, R. E., Roth, S. E., & Dymond, J. (1990). Near-inertial motions over a mid-ocean ridge: Effects of topography and hydrothermal plumes. *Journal of Geophysical Research*, 95(C5), 7261. <https://doi.org/10.1029/jc095ic05p07261>
- Thomson, R. E., & Emery, W. J. (2014). *Data Analysis Methods in Physical Oceanography: Third Edition*. In *Data Analysis Methods in Physical Oceanography: Third Edition (Third)*. <https://doi.org/10.1016/C2010-0-66362-0>
- Thomson, R. E., & Krassovski, M. V. (2015). Remote alongshore winds drive variability of the California Undercurrent off the British Columbia-Washington coast. *Journal of Geophysical Research: Oceans*, 120(12), 8151–8176. <https://doi.org/10.1002/2015JC011306>
- Xie, X., & Chen, D. (2021). Near-surface reflection and nonlinear effects of low-mode internal tides on a continental slope. *Journal of Physical Oceanography*, 51(4), 1037–1051. <https://doi.org/10.1175/JPO-D-20-0197.1>
- Xie, X., Liu, Q., Zhao, Z., Shang, X., Cai, S., Wang, D., & Chen, D. (2018). Deep Sea Currents Driven by Breaking Internal Tides on the Continental Slope. *Geophysical Research Letters*, 45(12), 6160–6166. <https://doi.org/10.1029/2018GL078372>
- Zheng, J., Tian, J., & Liang, H. (2017). Observation of near-inertial internal waves on the continental slope in the northwestern South China Sea. *Journal of Ocean University of China*, 16(2), 184–190. <https://doi.org/10.1007/s11802-017-3153-7>